UDC 621.314 https://doi.org/10.20998/2074-272X.2024.6.11

M. Si Ahmed, Y. Guettef, A. Mokaddem, A. Mokhefi, A. Hamid, P. Spiteri, F.Z. Medjaoui

Design optimization for enhancing performances of integrated planar inductor for power electronics applications

Goal. *In this work, the performance of an integrated planar inductor with a square geometric shape using different materials for the substrate: Ni-Fe, Mn-Zn and Ni-Zn have been analyzed and investigated in order to assess the impact of the substrate material on the performance of the integrated planar inductor and to determine the optimal material in the various applications of power modules in power electronics.* ***Methods****. To this end, we carried out an in-depth analysis of the geometric dimensions of the integrated planar inductor, by calculating all the geometric parameters of the proposed structure, to establish an equivalent physical model of the integrated planar inductor in order to evaluate its different electrical specifications. The numerical simulation, based on the three-dimensional mathematical model of the system using Maxwell's equations, was realized by COMSOL Multiphysics software.* ***Results*** *show the importance of the substrate material for the performance of the integrated planar inductor, and specify that the use of Ni-Fe ferrite as a substrate of the integrated planar inductor gives very interesting performance compared to other materials studied. The presented results provide valuable information on the influence of substrate material on the performance of embedded integrated planar inductor and can help to design and optimize these components for use in power electronic systems.* ***Practical value.*** *These results are significant for a wide range of applications, where the integrated planar inductor performance and efficiency can have a significant impact on the overall performance and cost-effectiveness of the power electronic device.* References 37, tables 2, figures 7.

Key words: **integrated square micro-coil, electrical characteristics, thermal modeling, electromagnetic phenomena, substrate material.**

Мета*. У цій роботі проаналізовано та досліджено характеристики вбудованого планарного індуктора квадратної геометричної форми з використанням різних матеріалів підкладки: Ni-Fe, Mn-Zn та Ni-Zn для оцінки впливу матеріалу підкладки на продуктивність вбудованого планарного індуктора та визначення оптимального матеріалу для різних силових застосувань модулів у силовій електроніці.* ***Методи****. З цією метою проведено поглиблений аналіз геометричних розмірів вбудованого планарного індуктора, розраховано всі геометричні параметри запропонованої конструкції для встановлення еквівалентної фізичної моделі вбудованого планарного індуктора та оцінки його електричних характеристик. Чисельне моделювання, що базується на тривимірній математичній моделі системи з використанням рівнянь Максвелла, було реалізовано за допомогою COMSOL Multiphysics.* ***Результати*** *показують важливість матеріалу підкладки для роботи вбудованого планарного індуктора і вказують на те, що використання фериту Ni-Fe у якості підкладки вбудованого планарного індуктора дає дуже цікаві характеристики порівняно з іншими вивченими матеріалами. Представлені результати надають важливу інформацію щодо впливу матеріалу підкладки на характеристики вбудованого планарного індуктора та можуть допомогти спроєктувати та оптимізувати дані компоненти для використання у силових електронних системах.* ***Практична цінність****. Отримані результати важливі для широкого спектра застосувань, де продуктивність та ефективність вбудованого планарного індуктора можуть істотно вплинути на загальну продуктивність та економічну ефективність силового електронного пристрою.* Бібл. 37, табл. 2, рис. 7.

Ключові слова: **вбудована квадратна мікрокотушка, електричні характеристики, теплове моделювання, електромагнітні явища, матеріал підкладки.**

1. Introduction. The advantages of integrating passive components, in particular integrated planar inductor, in power electronics are multiple and numerous, namely: improved performance and better profitability in a wide range of power electronics applications, including static converters and power systems. The low weight and small size of integrated planar inductor make them particularly suitable for use in compact and lightweight power electronics converters where they can reduce the overall size and weight of the device while improving its performance [1–4]. The integration of planar inductors makes it possible to add other functions on a single chip, more efficient designs and simplifying the manufacturing process [5, 6]. To this end, researchers are exploring various approaches to optimize the design and performance of integrated planar inductor, including the use of new materials, new advanced manufacturing techniques and innovative design methodologies [7]. These efforts allow the adoption of integrated planar inductor in complex power electronic systems, and further improve the efficiency, performance and profitability of the systems produced [8].

The integrated planar inductor is particularly used in low-power converters operating at high frequencies [9, 10]. Where they can be used to transform and transfer electrical energy efficiently with low losses. The choice of substrate material is an important factor in the design and optimization of integrated planar inductors [11, 12], as different materials can exhibit different electrical, magnetic and mechanical properties which can impact on the performance of the integrated planar inductor in terms of efficiency, stability and response time [13–16]. The best choice of the substrate material and its optimal parameters for the design of low-power converters is a crucial factor in order to improve the energy efficiency and the performance of the designed systems [17–23], the integrated planar inductor must be able to transfer energy with high efficiency and low losses, while preserving good stability and an ideal response time [19–26].

The experimental and numerical studies during the design phase of electronic equipment allow the understanding of the magneto-thermal behavior of its equipment and the optimization of their designs and guarantee of their performance and safety. In order to realize the circuits and electronic components with improved performance, it is essential to know all the electrical and thermal properties, which help to predict and understand the local temperature conditions and optimize the design of its components [27, 28]. In this context, the several methods have been used to study the electrical and thermal properties of electronic devices, for example, the finite-element method has been used to numerically study the thermal behavior of a circular-coil

inductor integrated in a micro DC-DC step-down converter [29–35]. In [32] investigated the temperature-dependent characteristics of cryogenic planar multilayer inductors. The autors [6, 32] predicted by numerical simulation the thermal-magnetic behavior of a square planar coil placed between two magnetic materials. In [34], the authors conducted a theoretical study on the design of an octagonal planar inductor and transformer for use in a converter, with the aim of improving the performance and efficiency of the conversion system. Overall, these research efforts have contributed to a better understanding of the electrical and thermal behavior of electronic equipment and have enabled the development of more efficient and better performing devices.

Goal. The work aim is to investigate, analyze and compare the performance of an integrated planar inductor with a planar topology of square geometric shape using three different materials for the substrate: Ni-Fe, Mn-Zn and Ni-Zn, in order to evaluate the impact of the best substrate material on the performance of the integrated planar inductor and identify the best performing material in terms of increasing the efficiency, stability and response time of the integrated planar inductor as well as their optimal design parameters in order to obtain the best performance of the integrated planar inductor.

The results of this study will undoubtedly provide useful information to experimenters on the influence of substrate material, the performances of the integrated planar inductor and present the design and optimization of these components for use in a wide range of specific power electronics applications.

It should be noted that the various numerical models proposed by the researchers often assume a stable state of the ambient air and tend to focus on the electrical and magnetic aspects of the passive components. Our main contribution is to provide a new thermal model that takes into account the real effects of buoyancy on the thermal behavior of a square integrated planar inductor using COMSOL software [36, 37]. Additionally, this study includes the effect of coil conductor width on electromagnetic and thermal properties by mathematically coupled the Navier-Stokes momentum and Maxwell's electromagnetism equations.

The current state of research in the field of integrated planar inductors for power electronics applications mostly ignores the effects of air motion and buoyancy on thermal behavior. The numerical models proposed by researchers often assume a stable state of the surrounding air and tend to focus on the electrical and magnetic aspects of passive components. The aim of this study is to provide a new thermal model that takes into account the real effects of buoyancy on the thermal behavior of a planar micro-coil. Additionally, this study investigates the effect of the width of the coil conductor on the electromagnetic and thermal properties. This research aims to offer a more realistic view of thermal phenomenon in electrical equipment by mathematically coupling of Navier-Stokes momentum equations and Maxwell's electromagnetism.

2. Development of a physical model for the micro-coil.

2.1. Defining the study area. Micro-coil Modeling. The current study focuses on the examination of a planar micro inductor with a square spiral shape, the performance of a planar inductor depends on its geometric parameters such as the number of turns (n), inner diameter (d_{in}), outer diameter (d_{out}), initial width (w_i), final width (w), thickness (t), and total length (L_t). This micro-coil is placed on a ferrite substrate that also has a square shape with a side length of L and thickness of t_{sub}. Additionally, the micro-coil is elevated by a height of H.

2.2. Determining the geometric parameters of inductors for calculation. In order to optimize the geometric characteristics of an inductor, to improve its performance, the several methods and mathematical models have been used for this purpose. Among these methods, the calculation method developed by Wheeler [14] makes it possible to evaluate the inductance for coils of hexagonal, octagonal or square shapes, which are built using discrete methods. This theoretical model is easy to implement, thanks to its accuracy compared to other methods and will always remain valid even for coils with a limited number of turns. The geometrical parameters of the micro-coil and the substrate are detailed in Fig. 1, and the specific values used in this investigation are listed in Table 1.

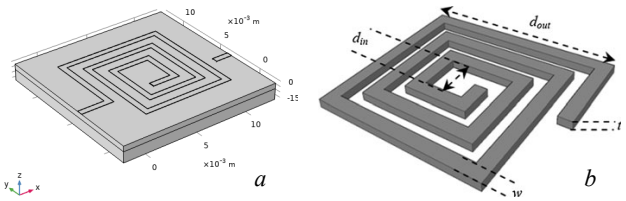

Fig. 1. Study area of the micro-coil deposited on substrate (*a*) geometrical parameters of the micro-inductor (*b*)

Table 1

The recommended parameters

Inner diameter d_{in}, mm	3	Spires thickness t, µm	35
Outer diameter d_{out}, mm	10	Spires number n	3
Spires width w, mm	0.55	Turn spacing s, µm	925

From a specification, we will size, using Wheeler's modified method, the square spiral coil, in order to minimize losses [35]. Additionally, the physical and electrical parameters of the different materials involved in Fig. 2 [3] including air, copper and ferrite are also given in Table 2.

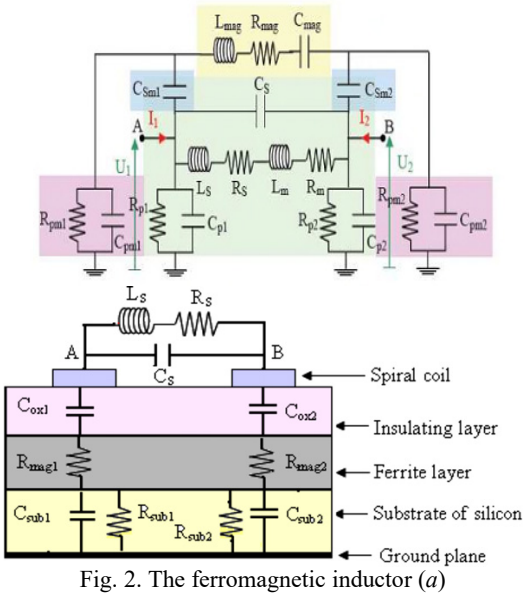

Fig. 2. The ferromagnetic inductor (*a*) and cross-section of planar inductor on ferrite (*b*)

Table 2

The physical and electrical parameters of different components

Properties	Air	Copper	Ni-Fe (sub1)	Mn-Zn (sub2)	Ni-Zn (sub3)
Density γ, kg/m^3	1.225	8700	4000	4700	4800
Viscosity η, Pa·s	$1.8\cdot10^{-5}$	–	–	–	–
Thermal conductivity k, W·m^{-1}·K^{-1}	0.0257	400	30	3.9	6.3
Heat capacity C, J·kg^{-1}·K^{-1}	1005.4	385	700	1050	710
Electrical resistivity ρ, Ω·m	$1.3\cdot10^{16}$	$1.75\cdot10^{-8}$	–	–	–
Relative permittivity ε_r	1.0	1.0	11.8	270	12
Relative permeability μ_r	1.0	1.0	800	5000	1500
Thermal expansion α, K$^{-1}\cdot10^{-3}$	3.43	–	–	–	–

3. Mathematical formulation of the problem.

3.1. Basic mathematical equations. The inductance L given by Wheeler method is represented by:

$$L = k_1 \cdot \mu_0 \cdot \frac{n^2 \cdot d_{avg}}{1 + k_2 \cdot A_m}, \quad (1)$$

where d_{avg} is the average diameter; A_m is the form factor; n is the number of turns; μ_0 is the vacuum permeability.

By using the Wheeler method for the square shape, the coefficients $k_1 = 2.34$, $k_2 = 2.75$. So we have:

$$d_{avg} = (d_{out} + d_{in}) / 2; \quad (2)$$

$$A_m = (d_{out} - d_{in}) / (d_{out} + d_{in}). \quad (3)$$

Based on the form factor A_m, we have the option to create either hollow or full inductors. Consequently, the hollow inductor exhibits higher inductance than a full one due to the turns situated near the center of the spiral, which help to reduce the positive mutual inductances and increase the negative mutual inductances [12].

The electric current i flowing through the conductors is dependent on both the current density J_{avg} and the cross-sectional area S_c of the conductor:

$$i = S_c \cdot J_{avg}. \quad (4)$$

The cross-sectional area is determined by the width w and the thickness t of the planar coil:

$$S_c = w \cdot t. \quad (5)$$

The spacing between turns is given by:

$$s = \frac{d_{out} - d_{in} - 2 \cdot w \cdot n}{2 \cdot (n-1)}. \quad (6)$$

The width w is equal to

$$w = \frac{d_{out} - d_{in} - 2 \cdot s \cdot (n-1)}{2 \cdot n}. \quad (7)$$

And the total lengths l_t:

$$l_t = 4 \cdot n \cdot (d_{out} - s \cdot (n-1) - n \cdot w) - s. \quad (8)$$

In this study, a mathematical model was developed to understand the behavior of integrated micro-coil. The model combines Maxwell's equations for electrical and magnetic phenomena with a thermal conduction equation to determine the temperature profile in the coil conductors. Additionally, to take into account the effect of air on the thermal performance, a computational fluid dynamics approach was used. This approach considers the convective heat transfer and includes the Navier-Stokes equations for laminar flow that are strongly coupled with the convection-diffusion equation for air. The buoyancy term of the air is introduced in the Navier-Stokes momentum (11) in the direction along the vertical Z (Fig. 1,*a*). The resulting mathematical model is a strong coupling between the Maxwell's equations, the combined convection-conduction equation of the air, and the Navier-Stokes momentum equation.

Maxwell's equations are:

$$\begin{aligned} &\boldsymbol{J} = \nabla \times \boldsymbol{H}; \quad \boldsymbol{B} = \nabla \times \boldsymbol{A}; \quad \boldsymbol{E} = -j\omega \boldsymbol{A}; \\ &\boldsymbol{J} = \sigma \boldsymbol{E} + j\omega \boldsymbol{D}; \quad \nabla \cdot \boldsymbol{J} = 0; \quad \boldsymbol{E} = -\nabla V - j\omega \boldsymbol{D}, \end{aligned} \quad (9)$$

where $\boldsymbol{H}$ is the magnetic field intensity; $\boldsymbol{J}$ is the current density; $\boldsymbol{B}$ is the magnetic flux density; $\boldsymbol{A}$ is the magnetic vector potential; $\boldsymbol{E}$ is the electric field intensity; ω is the angular frequency; σ is the electrical conductivity; $\boldsymbol{D}$ is the electric displacement field; V is the electric potential.

Heat equation in the air and the solid parts:

$$k_s \nabla^2 T_s + \rho_0 \boldsymbol{J} \otimes \boldsymbol{J} = 0 \quad \text{with } k_s = k_{Cu} \text{ or } k_s = k_{sub}, \quad (10)$$

where k_s is the thermal conductivity of the solid; k_{Cu} is the thermal conductivity of the copper; k_{sub} is the thermal conductivity of the substrate; T_s is the temperature in the solid; ρ_0 is the mass density of the solid.

Navier-Stokes equations in air part:

$$\begin{aligned} &\rho_{air} (\boldsymbol{u} \cdot \nabla) \boldsymbol{u} = -\nabla \cdot (P\boldsymbol{I}) + \left(\nabla \boldsymbol{u} + (\nabla \boldsymbol{u})^T\right) + \\ &+ A \rho_{air} \beta \boldsymbol{g} (T - T_c) \boldsymbol{e}, \end{aligned} \quad (11)$$

where ρ_{air} is the mass density of the air; $\boldsymbol{u}$ is the velocity of the flow of the air; P is the pressure in the air; $\boldsymbol{I}$ is the identity matrix; A is the coefficient for the buoyancy term; β is the thermal expansion coefficient; $\boldsymbol{g}$ is the gravitational acceleration; T is the temperature of the air; T_c is the reference temperature; $\boldsymbol{e}$ is the unit vector in the direction of gravitational force.

Heat equation in the air parts:

$$\rho_{air} Cp_{air} \cdot \boldsymbol{u} \cdot \nabla T = k_{air} \nabla^2 T, \quad (12)$$

where Cp_{air} is the specific heat capacity of air at constant pressure; k_{air} is the thermal conductivity of air.

The coupling between the electromagnetic, thermal, and Navier-Stokes equations involves several steps: solving Maxwell's equations to obtain the electric field and current density, calculating heat generation in solid materials due to Joule heating, solving the heat equation in solid materials to determine temperature distribution, solving the Navier-Stokes equations to find airflow around the inductor, and solving the heat equation in the air to account for convective heat transfer, using the velocity field obtained from the Navier-Stokes equations.

3.2. Boundary conditions. The solving of the above system equations (9)–(12) requires the boundary conditions such as:

- For the copper conductor:

- On the input:

$$I = I_0 \quad \text{or} \quad \boldsymbol{J} = I_0 / S_{via}, \quad (13)$$

where I is the the electric current; I_0 is the input current at the boundary of the copper conductor; $\boldsymbol{J}$ is the current density; S_{via} is the cross-sectional area.

- On the output:

$$V = 0. \quad (14)$$

This boundary condition implies that the electric potential is zero at the output boundary.

- At the copper boundary:

$$n \cdot J = 0, \quad -k_{Cu} \partial n T_s = h \cdot (T_c - T_s), \quad \text{and} \quad T = T_s, \quad (15)$$

where $n \cdot J$ – this boundary condition implies that there is no normal component of the current density at the boundary, meaning there is no current flowing out of the surface perpendicular to the boundary; k_{Cu} is the thermal conductivity of the copper material; $\partial n T_s$ – this boundary condition implies that there is no normal component of

the current density at the boundary, meaning there is no current flowing out of the surface perpendicular to the boundary; h is the convective heat transfer coefficient; T_c is the temperature of the surrounding air; T_s is the temperature at the surface of the copper conductor; T is the general temperature variable.

• At the substrate boundary:

$$-k_{sub}\partial nT_s = h\cdot(T_c - T_s), \quad \partial nT = 0, \quad \text{and} \quad u = 0, \qquad (16)$$

where k_{sub} is the thermal conductivity of the substrate material; u – this boundary condition suggests that the velocity of the air is zero at the substrate boundary, indicating a no-slip condition.

• At the study domain boundary:

$$\partial nT = 0, \quad \text{and} \quad P = 0, \qquad (17)$$

where P is the pressure.

4. Numerical and computational methods. The system of governing differential equations (9)–(12), along with the set of boundary conditions (13)–(17), has been solved using the finite element method with Galerkin discretization. For the mesh, we have employed a tetrahedral structure with prisms at the boundary layer (coil and substrate). The multiple tests carried out to ensure result independence have led us to adopt a fine tetrahedral irregular mesh for the coil conductor. The complete mesh consists of 29,888 domain elements and 1,172 boundary elements (Fig. 3). The convergence criterion is set to a relative error of each variable, ensuring their values below 10^{-6}.

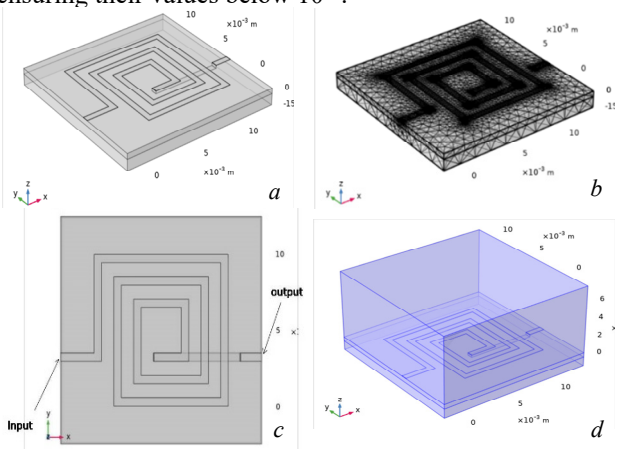

Fig. 3. The physical model (*a*), mesh of micro-coil (*b*), scheme for initial conditions (*c*) and limits of the studied area (*d*)

To ensure the accuracy and reliability of our numerical results, we conducted a comparison with the previous work [34]. We added their simulation conditions to examine the temperature distribution in the study area and along the vertical line passing through the substrate, as depicted in Fig. 4, 5. Upon comparing of our findings with the reference results [34], we observed the strong agreement and consistency, thereby validating of our mathematical model.

The simulation results obtained by solving the Maxwell's equations are applicable to all of the configurations studied. Therefore, in this study we will only focus on presenting the unique physical models and boundary conditions for each case. Figures 3,*a–d* depict the physical model of the square planar coil, the domain mesh, and the initial and boundary conditions, respectively.

4.1. Distribution of magnetic flux density. Figure 4 shows the 3D distribution of the magnetic flux density in planar coil for three materials of ferrite (Ni-Fe, Mn-Zn and Ni-Zn).

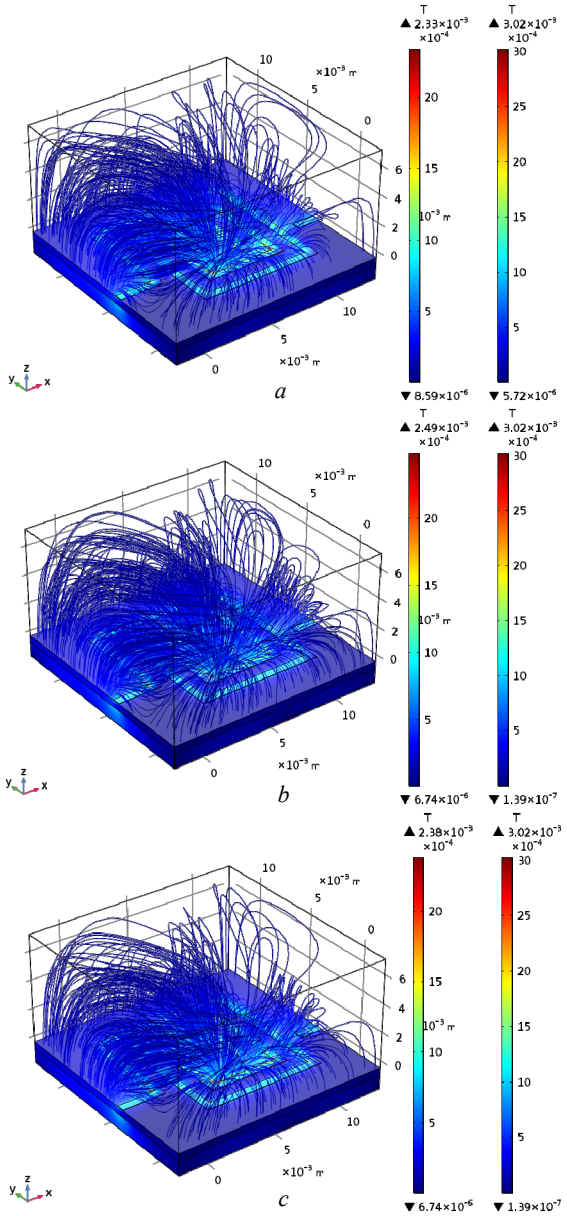

Fig. 4. The distributions of magnetic flux density for Ni-Fe (*a*), Mn-Zn (*b*) and Ni-Zn (*c*)

Figure 4 illustrates the magnetic flux density distribution along the median line ($x = y = 0$) for the micro-inductor made of materials Mi-Zn, Ni-Zn and Ni-Fe. The decreasing of the inner width of the micro-coil results in an increase in the flux value, it particularly evident in the region between 2 mm and 3 mm, corresponding to the line crossing the plane of the micro-coil. The similar magnetic behavior is observed in the neighboring zones with lower variance rates.

To further analyze the effect of changing the inner width of the micro-inductance on electromagnetic behavior, we have plotted curves that show casing variations in key parameters like maximum flux density, maximum field modulus, and maximum potential. The same figure illustrates the distribution of maximum magnetic flux density and maximum electric field for the inner width of the inductor (w = 0.6 mm). It reveals a evident increase in magnetic flux with decreasing w and predominant increase in the maximum electric field. The active zone of direct influence of the electric field is observed when the internal width is below 0.3 mm.

4.2. Temperature distribution. Regarding the temperature evolution in the study area, it is essential to plot the temperature distribution curves along the lines defined in the next diagrams. This is evident in Fig. 5, where we observe a rapid temperature increase in the kapton material along the median line ($x = y = 0$). The temperature is sharp until it reaching a peak at the micro-coil plane, exhibiting a perfect fit. This behavior can be attributed to the influence of the buoyancy force.

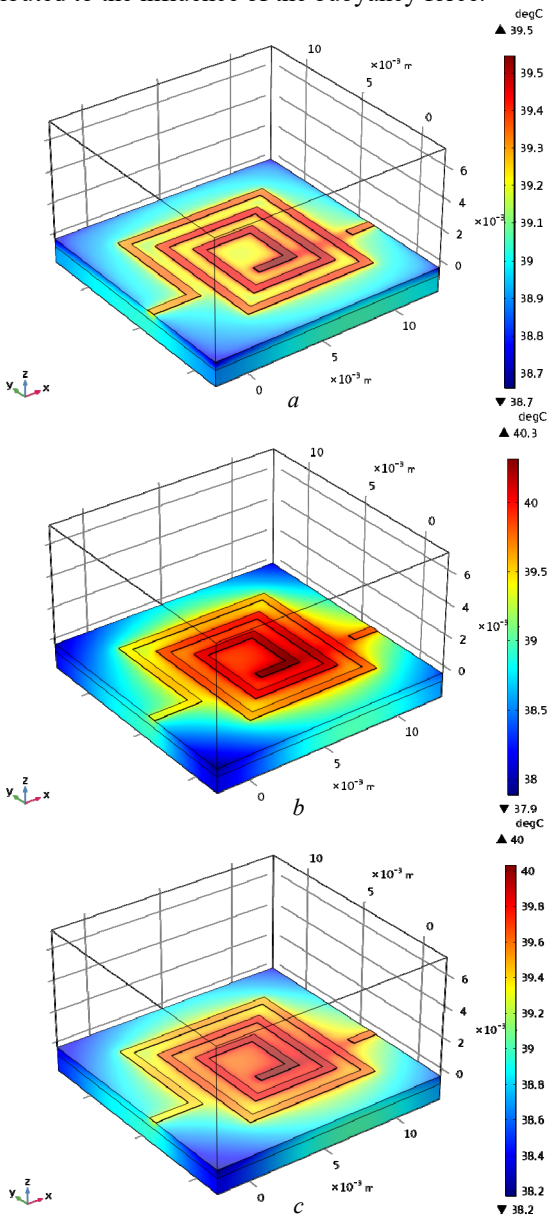

Fig. 5. The temperature distributions for Ni-Fe (*a*), Mn-Zn (*b*) and Ni-Zn (*c*)

As we move upward, the temperature begins to decrease, and a slight difference between the two curves becomes evident, indicating the minor effect of the buoyancy force in this particular region. Along the lateral line shown in Fig. 5, a noticeable change in the thermal distribution shape occurs, particularly at the plane where the coil turns are placed. The thermal peak rises at non-availability of buoyancy, and then the curves start to diverge by 1 °C as they move upward, with natural convection resulting in the lowest temperatures. The temperature distribution on the horizontal line presented in Fig. 5 confirms the earlier observation regarding the narrowing of the isothermal lines. We observe a reduction of the temperature values on both sides above the coil, where the maximum temperature value is directly recorded on the area of the inner diameter of the coil in both cases, with a higher value for this peak when considering the buoyancy force.

4.3. Comparison between three materials on the temperature and the flux magnetic distribution. The flux magnetic density and temperature distribution were compared for three different ferrite materials: Ni-Fe, Mn-Zn and Ni-Zn (Fig. 6, 7). In terms of magnetic flux density, it was observed that Mn-Zn exhibited the highest magnetic flux density, followed by Ni-Zn and Ni-Fe. The differences in magnetic flux density were attributed to the varying magnetic properties of the different ferrite materials.

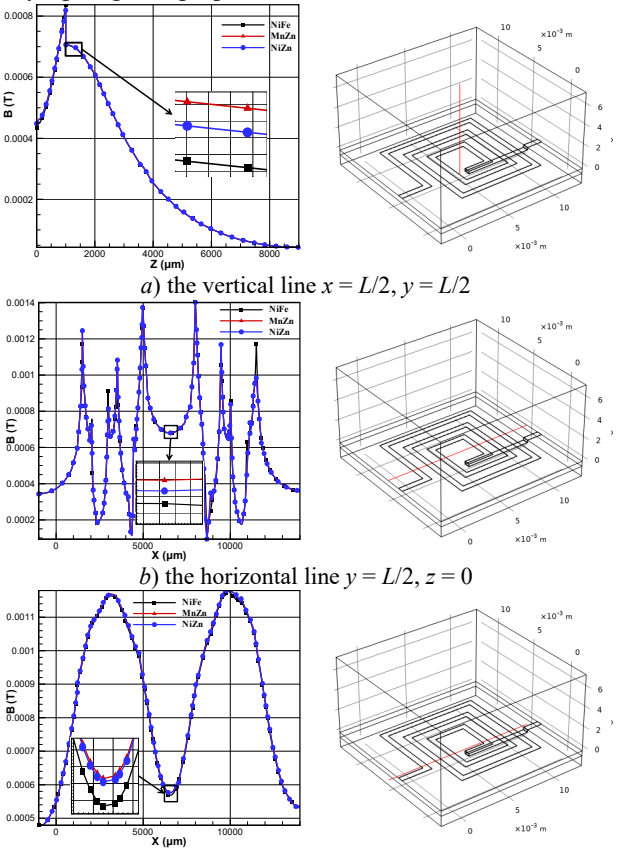

a) the vertical line $x = L/2$, $y = L/2$

b) the horizontal line $y = L/2$, $z = 0$

c) the horizontal line $y = L/2$, $z = -t_k - t_s/2$

Fig. 6. The comparison between three ferrite materials (Ni-Fe, Mn-Zn and Ni-Zn) on flux magnetic density

Regarding the temperature distribution, the results showed that Ni-Fe had the lowest temperature, indicating better thermal performance compared to the other two materials. Ni-Zn had a moderate temperature distribution, while Mn-Zn exhibited the highest temperature, indicating relatively poorer thermal behavior.

Summarizing the comparison between the three ferrite materials, Mn-Zn exhibited the highest magnetic flux density but also the highest temperature distribution, indicating potential trade-offs between magnetic performance and thermal behavior. Ni-Fe, on the other hand, showed the lowest temperature distribution, making a favorable choice for applications where thermal considerations are crucial. Ni-Zn is between the two materials, offering a balanced compromise between magnetic and thermal properties. The selection of the most suitable ferrite material would depend on the specific requirements of the application, considering factors such as magnetic performance, temperature sensitivity and overall efficiency.

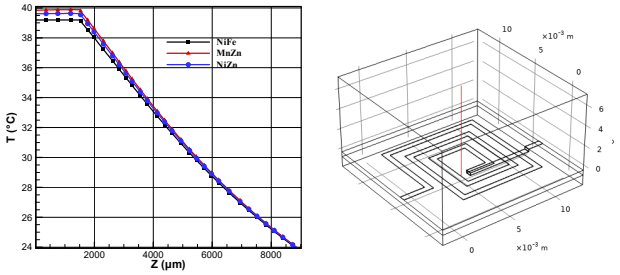

a) the vertical line $x = L/2$, $y = L/2$

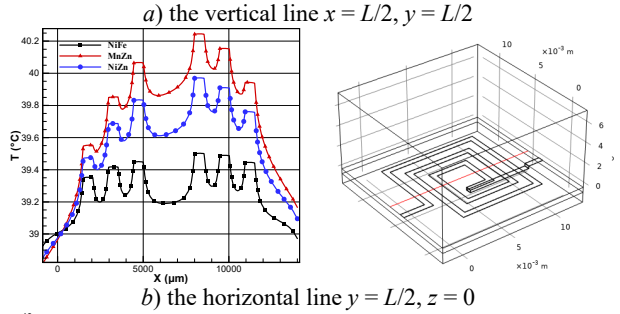

b) the horizontal line $y = L/2$, $z = 0$

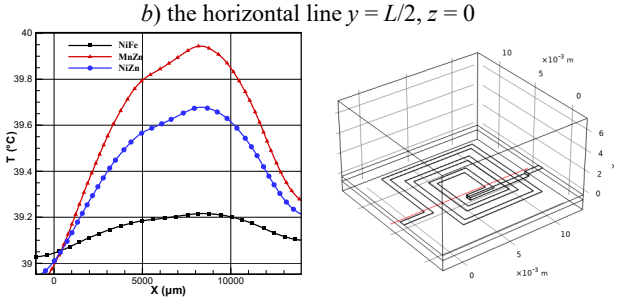

c) the horizontal line $y = L/2$, $z = -t_k - t_s/2$

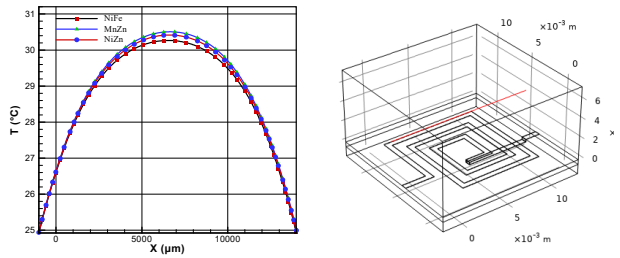

d) the horizontal line $y = L/2$, z= height air/2

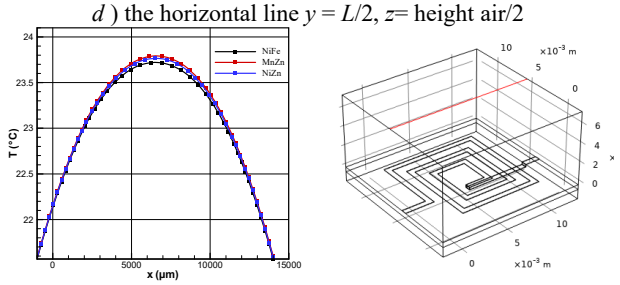

e) the horizontal line $y = L/2$, z = height air

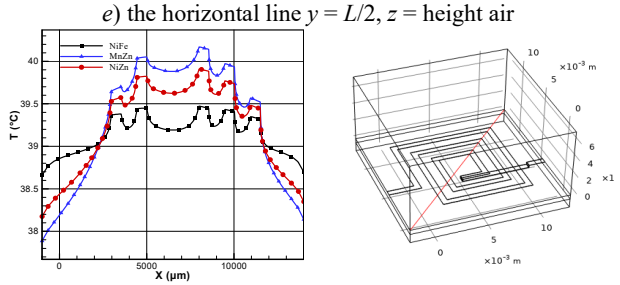

f) the diagonal line $z = 0$

Fig. 7. The comparison between three ferrite materials (Ni-Fe, Mn-Zn and Ni-Zn) on the temperature distribution

5. Conclusions. After conducting an in-depth study on the magnetic and thermal properties of three ferrite materials (Ni-Fe, Mn-Zn, Ni-Zn) we have found valuable characteristics regarding their performance and behavior across diverse applications.

Firstly, Mn-Zn emerged as the preferential material in terms of magnetic flux density, showing the highest values among the three. This exceptional magnetic performance holds immense significance for applications like transformers and inductors, where upper magnetic properties are crucial for optimal efficiency and performance.

Secondly, our observations of the temperature distribution revealed significant distinctions among the materials. Ni-Fe exhibited the lowest temperature distribution; giving the exceptional thermal performance compared to the other two. Its ability to efficiently dissipate heat makes it as the best choice for applications where thermal considerations play a basic role, such as high-power integrated circuits, where temperature management is critical for reliability.

On the other hand, Ni-Zn displayed a moderate temperature distribution, striking a favorable balance between the magnetic performance of Mn-Zn and the thermal performance of Ni-Fe. This characteristic makes Ni-Zn a viable option for applications demanding a harmonious convergence of both magnetic and thermal properties.

Nonetheless, when selecting the most suitable ferrite material, the careful consideration of specific application requirements becomes essential. Factors like the required magnetic flux density, temperature sensitivity, thermal constraints and energy losses should be diligently evaluated to ensure optimal performance in the intended application.

As a conclusion, this comprehensive study facilitated an in-depth comparison of Ni-Fe, Mn-Zn and Ni-Zn ferrite materials, their different magnetic flux density and temperature distribution characteristics. Each material presents unique advantages and drawbacks, and the optimal choice relies on the precise demands of the application. Our research significantly contributes to advancing our understanding of ferrite material properties and proposes the potential to optimize the design of electronic and electromagnetic systems, enhancing overall efficiency and performance. Moving forward, future research can further explore the additional properties of ferrite materials and their specific impacts on applications, expanding the boundaries of technological innovation to achieve even more advanced solutions.

Conflict of interest. The authors declare that they have no conflicts of interest.

REFERENCES

1. Kharbouch H., Guettaf Y., Hamid A., Bley V., Benhadda Y. Design and Implementation of Inductors with Variable Conductor Width Integrated in a Boost Micro Converter. *Transactions on Electrical and Electronic Materials*, 2021, vol. 22, no. 4, pp. 519-530. doi: https://doi.org/10.1007/s42341-020-00261-5.

2. Guettaf Y., Flitti A., Bensaci A., Kharbouch H., Rizouga M., Hamid A. Simulation of the operation of a DC–DC converter containing an inductor of planar type. *Electrical Engineering*, 2018, vol. 100, no. 2, pp. 953-969. doi: https://doi.org/10.1007/s00202-017-0558-7.

3. Derkaoui M., Benhadda Y., Hamid A. Modeling and simulation of an integrated octagonal planar transformer for RF systems. *SN Applied Sciences*, 2020, vol. 2, no. 4, art. no. 656. doi: https://doi.org/10.1007/s42452-020-2376-1.

4. Namoune A., Taleb R., Mansour N., Benzidane M.R., Boukortt A. Integrated through-silicon-via-based inductor design in buck converter for improved efficiency. *Electrical Engineering & Electromechanics*, 2023, no. 6, pp. 54-57. doi: https://doi.org/10.20998/2074-272X.2023.6.09.

5. Xu D., Guan Y., Wang Y., Wang W. A review of high frequency resonant DC-DC power converters: Topologies and planar magnetic technologies. *Science China Technological Sciences*, 2020, vol. 63, no. 8, pp. 1335-1347. doi: https://doi.org/10.1007/s11431-020-1665-3.

6. Medjaoui F.Z., Hamid A., Guettaf Y., Spiteri P., Bley V. Conception and Manufacturing of a Planar Inductance on NiFe Substrate. *Transactions on Electrical and Electronic Materials*, 2019, vol. 20, no. 3, pp. 269-279. doi: https://doi.org/10.1007/s42341-019-00105-x.

7. Kim S.-G., Yun E.-J., Kim J.-Y., Kim J., Cho K.-I. Microfabrication and characteristics of double-rectangular spiral type thin-film inductors

with an upper NiFe magnetic core. *Journal of Applied Physics*, 2001, vol. 90, no. 7, pp. 3533-3538. doi: https://doi.org/10.1063/1.1399026.
8. Liu X., Wang T., Gao F., Khan M.M., Yang X., Rogers D.J. A Resonant Inductor Integrated-Transformer-Based Receiver for Wireless Power Transfer Systems. *IEEE Transactions on Industrial Electronics*, 2023, vol. 70, no. 4, pp. 3616-3626. doi: https://doi.org/10.1109/TIE.2022.3174286.
9. Meshkat A., Dehghani R., Farzanehfard H., Khajehoddin S.A. Improved On-Chip Inductor Design for Fully Integrated Voltage Regulators. *IEEE Journal of Emerging and Selected Topics in Power Electronics*, 2022, vol. 10, no. 6, pp. 7397-7409. doi: https://doi.org/10.1109/JESTPE.2022.3199692.
10. Shaltout A.H., Gregori S. Layout optimization of planar inductors for high-efficiency integrated power converters. *Analog Integrated Circuits and Signal Processing*, 2020, vol. 102, no. 1, pp. 155-167. doi: https://doi.org/10.1007/s10470-019-01494-y.
11. Shetty C., Smallwood D.C. Design, Modeling, and Analysis of a 3-D Spiral Inductor With Magnetic Thin-Films for PwrSoC/PwrSiP DC-DC Converters. *IEEE Access*, 2022, vol. 10, pp. 92105-92127. doi: https://doi.org/10.1109/ACCESS.2022.3200335.
12. Jiao D., Ni L., Zhu X., Zhe J., Zhao Z., Lyu Y., Liu Z. Measuring gaps using planar inductive sensors based on calculating mutual inductance. *Sensors and Actuators A: Physical*, 2019, vol. 295, pp. 59-69. doi: https://doi.org/10.1016/j.sna.2019.05.025.
13. Freitas W.J., Manera L.T., Swart J.W. Functional cyclic bending test for integrated inductors on flexible Kapton substrate. *Microelectronics Reliability*, 2022, vol. 135, art. no. 114592. doi: https://doi.org/10.1016/j.microrel.2022.114592.
14. Khan F., Younis M.I. Investigation of on-chip integrated inductors fabricated in SOI-MUMPs for RF MEMS ICs. *Analog Integrated Circuits and Signal Processing*, 2020, vol. 102, no. 3, pp. 585-591. doi: https://doi.org/10.1007/s10470-020-01627-8.
15. Anthony R., Wang N., Casey D.P., Mathuna O.C., Rohan J.F. MEMS based fabrication of high-frequency integrated inductors on Ni–Cu–Zn ferrite substrates. *Journal of Magnetism and Magnetic Materials*, 2016, vol. 406, pp. 89-94. doi: https://doi.org/10.1016/j.jmmm.2015.12.099.
16. Murali P., Alvarez C., Suresh S., Losego M.D., Swaminathan M., Oishi Y., Uemura T., Nagatsuka R., Watanabe N. Semi-additive patterning process based fabrication of miniaturized, package-embedded high conversion ratio inductors for DC-DC converters. *Power Electronic Devices and Components*, 2022, vol. 3, art. no. 100023. doi: https://doi.org/10.1016/j.pedc.2022.100023.
17. Shetty C. A detailed study of Q_{dc} of 3D micro air-core inductors for integrated power supplies: Power supply in package (PSiP) and power supply on chip (PSoC). *Power Electronic Devices and Components*, 2022, vol. 2, art. no. 100006. doi: https://doi.org/10.1016/j.pedc.2022.100006.
18. Liu S., Zhu L., Allibert F., Radu I., Zhu X., Lu Y. Physical Models of Planar Spiral Inductor Integrated on the High-Resistivity and Trap-Rich Silicon-on-Insulator Substrates. *IEEE Transactions on Electron Devices*, 2017, vol. 64, no. 7, pp. 2775-2781. doi: https://doi.org/10.1109/TED.2017.2700022.
19. Ouyang Z., Thomsen O.C., Andersen M.A.E. Optimal Design and Tradeoff Analysis of Planar Transformer in High-Power DC–DC Converters. *IEEE Transactions on Industrial Electronics*, 2012, vol. 59, no. 7, pp. 2800-2810. doi: https://doi.org/10.1109/TIE.2010.2046005.
20. Zhang W., Su Y., Mu M., Gilham D.J., Li Q., Lee F.C. High-Density Integration of High-Frequency High-Current Point-of-Load (POL) Modules With Planar Inductors. *IEEE Transactions on Power Electronics*, 2015, vol. 30, no. 3, pp. 1421-1431. doi: https://doi.org/10.1109/TPEL.2014.2320857.
21. Musunuri S., Chapman P.L., Zou J., Liu C. Design Issues for Monolithic DC–DC Converters. *IEEE Transactions on Power Electronics*, 2005, vol. 20, no. 3, pp. 639-649. doi: https://doi.org/10.1109/TPEL.2005.846527.
22. Hsiang H.-I. Progress in materials and processes of multilayer power inductors. *Journal of Materials Science: Materials in Electronics*, 2020, vol. 31, no. 19, pp. 16089-16110. doi: https://doi.org/10.1007/s10854-020-04188-8.
23. Ahmed B., Yacine G., Rabah D., Hamid M.-H.-A. Design and electromagnetic modeling of integrated LC filter in a buck converter. *Facta Universitatis - Series: Electronics and Energetics*, 2020, vol. 33, no. 2, pp. 289-302. doi: https://doi.org/10.2298/FUEE2002289A.
24. Pordanjani S.R., Mahseredjian J., Naïdjate M., Bracikowski N., Fratila M., Rezaei-Zare A. Electromagnetic modeling of inductors in EMT-type software by three circuit-based methods. *Electric Power Systems Research*, 2022, vol. 211, art. no. 108304. doi: https://doi.org/10.1016/j.epsr.2022.108304.
25. Sagar P., Gour A.S., Karunanithi R. A multilayer planar inductor based proximity sensor operating at 4.2 K. *Sensors and Actuators A: Physical*, 2017, vol. 264, pp. 151-156. doi: https://doi.org/10.1016/j.sna.2017.07.042.
26. Zhou G., Zhang W., He D., Li X., Wang S., Hong Y., Chen Y., Wang C., He W., Miao H., Zhou J. A novel structured spiral planar embedded inductor: Electroless-plating NiCoP alloy on copper coil as magnetic core. *Journal of Magnetism and Magnetic Materials*, 2019, vol. 489, art. no. 165363. doi: https://doi.org/10.1016/j.jmmm.2019.165363.
27. Bechir M.H., Yaya D.D., Kahlouche F., Soultan M., Youssouf K., Capraro S., Chatelon J.P., Rousseau J.J. Planar inductor equivalent circuit model taking into account magnetic permeability, loss tangent, skin and proximity effects versus frequency. *Analog Integrated Circuits and Signal Processing*, 2016, vol. 88, no. 1, pp. 105-113. doi: https://doi.org/10.1007/s10470-016-0697-1.
28. Benhadda Y., Hamid A., Lebey T. Thermal Modeling of an Integrated Circular Inductor. *Journal of Nano- and Electronic Physics*, 2017, vol. 9, no. 1, art. no. 01004. doi: https://doi.org/10.21272/jnep.9(1).01004.
29. Rizou M.E., Prodromakis T. Electrothermal deterioration factors in gold planar inductors designed for microscale bio-applications. *Microelectronic Engineering*, 2018, vol. 197, pp. 61-66. doi: https://doi.org/10.1016/j.mee.2018.05.006.
30. Vellvehi M., Jorda X., Godignon P., Ferrer C., Millan J. Coupled electro-thermal simulation of a DC/DC converter. *Microelectronics Reliability*, 2007, vol. 47, no. 12, pp. 2114-2121. doi: https://doi.org/10.1016/j.microrel.2006.10.009.
31. Sagar P., Hassan H.K., Lakshmi E.D.A., Akber K., Girish P.S., Gour A.S., Karunanithi R. Investigation on Temperature Dependent Inductance (TDI) of a planar Multi-Layer Inductor (MLI) down to 4.2 K. *Review of Scientific Instruments*, 2020, vol. 91, no. 8. doi: https://doi.org/10.1063/5.0008901.
32. Medjaoui F.Z., Mokhfi A., Guettaf Y., Spetiri P., Hamid A. Magnetothermal behavior of a planar coil. *Transactions on Electrical and Electronic Materials*, 2022, vol. 23, no. 2, pp. 171-181. doi: https://doi.org/10.1007/s42341-021-00337-w.
33. Derkaoui M., Benhadda Y., Hamid A., Temmar A. Design and Modeling of Octagonal Planar Inductor and Transformer in Monolithic Technology for RF Systems. *Journal of Electrical Engineering & Technology*, 2021, vol. 16, no. 3, pp. 1481-1493. doi: https://doi.org/10.1007/s42835-021-00692-x.
34. Fatna B., Mokhefi A., Hamid A., Yacine G., Fatima Zohra M., Spiteri P. Numerical investigation of the thermal convective phenomenon around a circular micro-coil with variable internal width. *Production Engineering*, 2023, vol. 17, no. 5, pp. 653-668. doi: https://doi.org/10.1007/s11740-023-01195-6.
35. Namoune A., Taleb R., Mansour N. Simulation of an integrated spiral inductor and inter-digital capacitor in a buck micro converter. *Automatika*, 2023, vol. 64, no. 2, pp. 268-276. doi: https://doi.org/10.1080/00051144.2022.2142572.
36. Gans Š., Molnár J., Kováč D. Estimation of electrical resistivity of conductive materials of random shapes. *Electrical Engineering & Electromechanics*, 2023, no. 6, pp. 72-76. doi: https://doi.org/10.20998/2074-272X.2023.6.13.
37. Zablodskiy M.M., Pliuhin V.E., Kovalchuk S.I., Tietieriev V.O. Indirect field-oriented control of twin-screw electromechanical hydrolyzer. *Electrical Engineering & Electromechanics*, 2022, no. 1, pp. 3-11. doi: https://doi.org/10.20998/2074-272X.2022.1.01.

Received 19.04.2024
Accepted 27.05.2024
Published 21.10.2024

Mohammed Si Ahmed [1], *PhD Student,*
Yacine Guettaf [1], *Full Professor,*
Allel Mokaddem [1], *Full Professor,*
Abderrahim Mokhefi [2], *Full Professor,*
Azzedine Hamid [1], *Full Professor,*
Pierre Spiteri [3], *Full Professor,*
Fatima Zohra Medjaoui [4], *Associate Professor,*
[1] Centre Universitaire Nour Bachir El-Bayadh, Algeria,
e-mail: medsiahmed95@gmail.com (Corresponding Author)
[2] Ecole Nationale Polytechnique d'Oran, Algeria,
[3] Institut de Recherche en Informatique de Toulouse, France,
[4] Universite des Sciences et de la Technologie d'Oran Mohamed-Boudiaf, Algeria.

How to cite this article:
Si Ahmed M., Guettef Y., Mokaddem A., Mokhefi A., Hamid A., Spiteri P., Medjaoui F.Z. Design optimization for enhancing performances of integrated planar inductor for power electronics applications. *Electrical Engineering & Electromechanics*, 2024, no. 6, pp. 84-90. doi: https://doi.org/10.20998/2074-272X.2024.6.11